



# Multifunctional paraffin wax/carbon nanotube sponge composites with simultaneous high-efficient thermal management and electromagnetic interference shielding efficiencies for electronic devices

Xiang Lu<sup>a,b</sup>, Yongfeng Zheng<sup>a</sup>, Jinglei Yang<sup>b,\*\*</sup>, Jinping Qu<sup>a,\*</sup>

<sup>a</sup> Key Laboratory of Polymer Processing Engineering of the Ministry of Education, National Engineering Research Center of Novel Equipment for Polymer Processing, Guangdong Key Laboratory of Technique and Equipment for Macromolecular Advanced Manufacturing, South China University of Technology, Guangzhou, 510641, China

<sup>b</sup> Department of Mechanical and Aerospace Engineering, Hong Kong University of Science and Technology, Clear Water Bay, Kowloon, Hong Kong, China

## ARTICLE INFO

### Keywords:

Paraffin wax  
Carbon nanotube sponge  
Thermal management  
Electromagnetic interference

## ABSTRACT

As the operating speed and efficiency of electronic devices increase continuously, developing their thermal management and electromagnetic shielding capabilities has become extremely important. In this study, we prepared a paraffin wax/carbon nanotube sponge (PW@CNS) composite with simultaneous high-efficient thermal management and electromagnetic interference shielding functions via the simple vacuum impregnation method. The PW component functions as the phase change working substance for thermal management applications, and whereas the three-dimensional electrically conductive CNS component forms the matrix supporting the PW and a shielding structure against electromagnetic waves. The properties of PW@CNS are characterized by Fourier transform infrared spectroscopy (FT-IR), X-ray diffraction (XRD), differential scanning calorimetry (DSC) and thermal gravimetric analysis (TGA). Its latent heat and relative enthalpy efficiency during melting and freezing process are as high as 248.8 J/g and 247.7 J/g, and 96.2% and 96.3%, respectively. After 100 thermal cycles, the latent heat remained nearly constant, and the prepared PW@CNS exhibited the excellent thermal management behavior and electromagnetic interference (EMI) shielding effectiveness (SE). All the results indicate that this PW@CNS has great potential as a thermal management and electromagnetic interference shielding material for electronic devices.

## 1. Introduction

With rapid technological development, electronic devices tend to be miniaturized, integrated, functional and networked [1,2]. Due to the continuous increasing of operating speed and efficiency, much of the heat generated by electronic devices cannot be dissipated in time. As a result, their actual operating temperature exceeds the maximum allowable temperature, causing a decrease in their performance or even failure and damage [3–5]. In order to ensure their operational reliability and stability, and extend their service life, it is necessary to develop efficient and practical heat dissipation technology.

In recent years, due to the low cost, good stability, easy processing ability and corrosion resistance, polymer composites with high thermal conductivity have been widely studied as thermal interface materials or

the heat dissipation of electronic devices. Yang et al. [6] introduced boron nitride (BN) fillers to intrinsic liquid crystal epoxy resin (LCER) and prepared a BN/LCER thermally conductive composites via a simple casting method. Compared with the general bisphenol-A epoxy resin (0.19 W/mK), the thermal conductivity of these BN/LCER composites reached 1.02 W/mK. Using silicon carbide nanowires, reduced graphene oxide and cellulose nanofiber as assembly units, Song et al. [7] constructed vertically aligned filler networks through an ice-templated assembly strategy and prepared silicon carbide/reduced graphene oxide/silicone rubber thermally conductive composites by infiltrating the filler networks with silicone rubber. With only 1.84 vol% filler network, the thermal conductivity of the obtained composites reached as high as 2.74 W/mK, which is about 16 times than that of pure silicone rubber (0.17 W/mK). Li et al. [8] added 35 wt% boron nitride

\* Corresponding author.

\*\* Corresponding author.

E-mail addresses: [maeyang@ust.hk](mailto:maeyang@ust.hk) (J. Yang), [jpqu@suct.edu.cn](mailto:jpqu@suct.edu.cn) (J. Qu).

<https://doi.org/10.1016/j.compositesb.2020.108308>

Received 19 May 2020; Received in revised form 17 July 2020; Accepted 24 July 2020

Available online 31 July 2020

1359-8368/© 2020 Elsevier Ltd. All rights reserved.

nanosheets (BNNSs) into a polydimethylsiloxane (PDMS) matrix and obtained BNNSs/PDMS composites with 1.16 W/mK thermal conductivity. Although all the polymer thermal interface materials with high thermal conductivity can effectively promote heat diffusion in electronic devices, they cannot maintain the optimal operating temperature of electronic devices.

Phase change materials (PCMs) are a type of functional materials that can store and release a large amount of latent heat and maintain a constant temperature during the phase change process [9,10]. The PCMs can absorb the heat dissipated by the electronic device during operation, thereby maintaining the operating temperature of the electronic device near the phase change temperature of the PCMs [9,11]. By selecting a PCMs with suitable phase change temperatures, the temperature control requirements of different electronic devices can be met, thereby effectively maintaining the operating temperature of electronic device within a suitable range, ensuring its safe and stable operation and extending its service life. Paraffin wax (PW), as a typical organic 'solid-liquid' PCMs, has been widely studied and used in the field of thermal energy storage due to its low cost, high energy storage density, moderate phase transition temperature and excellent thermal stability [12,13]. The risks of leakage and low thermal conductivity during phase transition are the two major issues for its practical application. Recently, to overcome these two shortcomings, various strategies, including porous materials adsorbing [14–16], microcapsule coating [17,18] and high molecular weight polymer shaping [19–21] etc., have been proposed to prepare PW-based form stable PCMs (FSPCMs) with high thermal conductivity that can maintain the solid state and exhibit a relatively high heat transfer rate during phase transition. Wang et al. [15] added 20.0 wt% expanded graphite (EG) into the PW to enhance the heat transfer rate of PW. As a result, the thermal conductivity of the prepared PW/EG FSPCM remained as high as 6.42 W/mK after 100 thermal cycles. Umair et al. [16] proposed a facile strategy for preparing PW-based FSPCMs by loading PW into a biomass-derived three-dimensional carbon scaffold. The obtained PW exhibited high thermal conductivity (0.4 W/mK) and energy storage density (about 182.22 J/g). All the reported researches show that the adsorption of PW through porous materials with high thermal conductivity is an effective way to prepare highly thermally conductive PW-based FSPCMs. The prepared FSPCMs with high thermal conductivity via this approach are expected to be used in the efficient thermal management of electronic devices.

For electronic devices, in addition to ensuring their safe and stable operation in the best state via thermal management, shielding the interference of electromagnetic waves from outside and preventing the electromagnetic pollution from the generated electromagnetic waves to the surrounding environment is another urgent issue to be solved [22–24]. In recent years, one of the most efficient means of preparing light weight, flexible and high-performance polymer-based electromagnetic interference (EMI) shielding materials has involved constructing a conductive porous material skeleton and filling it with a polymer [25–30]. Zhu et al. [25] filled poly dimethylsiloxane (PDMS) into three-dimensional graphene foam with high electronic conductivity and introduced Fe<sub>3</sub>O<sub>4</sub> nanoparticles to prepare high-performance EMI shielding composites in the frequency range of 8.2–12.4 GHz. Liang et al. [27] used ultra-ordered honeycomb units derived from natural wood-derived porous carbon (WPC) skeletons as micro-reactors to construct ultra-light electrically conductive 3D MXene aerogels, and prepared the MXene aerogel/WPC composites with excellent EMI shielding effectiveness (SE).

Carbon nanotube sponge (CNS), as a 3D porous foam formed by the disordered overlapping of carbon nanotubes, has good elasticity, low density, high porosity, high specific surface area, high electrical conductivity and high thermal conductivity, and so on [31]. Due to these advantages, it has been widely used for oil-water separation [32–34], FSPCMs [35], electrically and thermally conductive composites [36,37], electromagnetic interference shielding [38,39] and other applications. Chen et al. [35] prepared a multifunctional PW/CNS FSPCM with high

electro-to-heat or photo-to-thermal storage efficiencies (40–60%). Chen et al. [38] reported epoxy/CNS nanocomposites with the remarkable electrical conductivity of 148 S/m and an outstanding EMI SE of around 33 dB; the CNS loading in these composites was only 0.66 wt%. Therefore, CNS is an excellent 3D porous material for preparing high-performance FSPCMs or high-performance polymer-based EMI shielding materials.

To the best of our knowledge, few studies have been reported on functional materials with simultaneous thermal management and EMI shielding functions. Thus, in this study, we prepared a PW/CNS composite with high electrical and thermal conductivities via the simple vacuum impregnation approach by employing CNS as the supporting framework and PW as the filling medium. Furthermore, the influence of this PW/CNS composite on the thermal management and EMI shielding for electronic devices are systematically discussed.

## 2. Experiment

### 2.1. Raw materials and preparation method of PW@CNS

Paraffin wax (OP44E) was purchased from Hangzhou Luer New Material Technology Co., Ltd. Carbon nanotube sponge (XFCN01, normal density is about 10 mg/cm<sup>3</sup>) was purchased from Jiangsu Xianfeng Nano Material Technology Co., Ltd., the inner diameter and outer diameter of carbon nanotube are about 10–20 nm and 30–50 nm, respectively.

The PW@CNS composite was prepared by a simple vacuum impregnation method. Briefly, a piece of CNS (about 15 mm × 10 mm × 3 mm,  $m_0 = 8.8$  mg) was put into the melted PW. The specimen was moved into an 80 °C vacuum oven for 12 h to achieve adsorption saturation. After that, it was placed on a sheet of filter paper, and then put into an 80 °C blast oven to remove the unadsorbed PW. During this process, we changed the filter paper every 2 h until no PW leaked from the specimen. Finally, the PW@CNS composite was obtained and weighed ( $m_1 = 309.7$  mg). The PW loading ( $w_f$ ) in the obtained PW@CNS composite was 97.2 wt%, as calculated using Eq. (1).

$$w_f = \frac{m_1 - m_0}{m_1} \times 100\% \quad (1)$$

### 2.2. Characterization

The Fourier-transform infrared spectra (FTIR) of pure PW, CNS and PW@CNS were recorded using a Spectrum 2000 instrument (USA) with KBr pellets in the range of 4000–400 cm<sup>−1</sup> and a resolution of 2 cm<sup>−1</sup> after 32 scans at room temperature. The morphologies of the CNS and PW@CNS were examined using a scanning electron microscope (SEM, Quanta FEG 250, FEI, USA) at an accelerating voltage of 5 kV, prior to the SEM tests, all surfaces were sputtered with gold to provide enhanced conductivity. The X-ray diffraction patterns of pure PW, CNS and PW@CNS were recorded at 5°/min from 5° to 50° using Bruker D8 Advance (Germany). The phase changes properties, including the melting and freezing temperature (defined as the peak temperature) and melting and freezing enthalpies (defined as the peak area), were investigated using a Netzsch 204c differential scanning calorimetry (DSC) instrument (Germany) between 0 °C and 100 °C at a rate of 10 °C/min. The DSC measurement uncertainties for temperature and enthalpy are 0.05 °C and 3.0%, respectively. The thermal stability of PW and PW@CNS were investigated using a thermal gravimetric analyser (TGA, Netzsch TG209, Germany) at 10 °C/min from 30 °C to 600 °C under a nitrogen atmosphere. The thermal reliability and reusability of the obtained PW@CNS composite was measured using a KSON KTHB-415TBS (China) high-low temperature chamber, over 100 melting/freezing thermal cycles from 10 °C to 90 °C at 5 °C/min increasing rates and a respective 3 min isothermal period at 10 and 90 °C. The electrical resistances (R) of PW and PW@CNS were measured using a Keithley

electrometer model 4200-SCS (USA), and their electrical conductivity ( $\sigma$ ) was calculated via Eq. (2)

$$\sigma = \frac{L}{S \times R} \quad (2)$$

where  $L$  and  $S$  are the length and cross-sectional area of the PW and PW@CNS rectangular sheet, respectively. The thermal diffusivities ( $\alpha$ ) of the PW and PW@CNS were determined by LFA 427 (NETZSCH, Germany), and their thermal conductivities ( $\lambda$ ) were calculated by Eq. (3)

$$\lambda = \alpha \times C_p \times \rho \quad (3)$$

where  $C_p$  and  $\rho$  are the heat capacity and density of the sample, respectively. The EMI SE were calculated according to the  $S$  parameters and the relative electromagnetic parameters measured on a Keysight PNA E5071C vector network analyser using the hollow cylinder rings (outer diameter is 7 mm, inner diameter is 3.04 mm and thickness is 2 mm) method under room temperature from 1.0 GHz to 18.0 GHz. According to the  $S$ -parameters, the reflection coefficient ( $R = |S_{11}|^2 = |S_{22}|^2$ ), transmission coefficient ( $T = |S_{12}|^2 = |S_{21}|^2$ ) and absorption coefficient ( $A = 1 - T - R$ ) can be calculated. Then, the SE of reflection ( $SE_R = -10\log(1-R)$ ) and SE of absorption ( $SE_A = -10\log(T/1-R)$ ), total SE ( $SE_T = -10\log T = SE_R + SE_A$ ) also can be calculated. The thermal management behavior of obtained PW@CNS composites was investigated under a simulated heat source, and the temperature of the samples during these periods were recorded using an infrared thermography camera (FLIR, SC 3000).

### 3. Results and discussions

#### 3.1. Chemical structure of PW@CNS

CNS, as an excellent 3D supporting skeleton, has been widely investigated in the field of light-driven and electro-driven FSPCMs due to its remarkable light absorption and electrical conductivity [35]. In this study, the PW@CNS composite with high electrical conductivity and thermal conductivity is prepared via the simple vacuum impregnation by employing CNS as the supporting skeleton and PW as the phase change working substance. The preparation schematic diagram is shown in Fig. 1 a. Compared with the obvious fluffy porous structure of CNS (Fig. 1 b), the pore structure of CNS is perfectly filled by PW in PW@CNS (Fig. 1 c). However, the continuous skeleton structure of CNS in PW@CNS is still clearly visible, which can provide the complete

electrical and thermal pathway for PW@CNS.

Fig. 1 (d) shows the digital pictures of PW@CNS during the leakage test, and Fig. 2 shows the PW@CNS quality at different leak times. Due to the weak adsorption capacity of melted PW on the surface of carbon nanotubes, at the beginning of the leak test, some melted PW transferred from the CNS surface to the filter paper (as shown in Fig. 1 d1, d2, d3). With increasing leak time, the mass of PW transferred from the CNS to the filter paper decreases every two hours, until it reaches 309.7 mg, and then it remains constant (Fig. 1 d4, d5). Moreover, after this point, there are no further PW leaks out from the PW@CNS composite, even under 50 g load (about 162 times the PW@CNS weight). This indicates that the obtained PW@CNS composite has excellent form stability. Based on Eq. (1), the PW loading in the PW@CNS composite is as high as 97.2 wt%, which is higher than most of the reported values in the literature. This shows that the obtained PW@CNS has high thermal energy storage density.

FTIR analysis is a typical and conventional means to characterizing the chemical interaction between PW and CNS in PW@CNS. Fig. 3 (a) shows the FTIR spectra of CNS, pure PW and obtained PW@CNS. In the FTIR spectra of PW, the characteristic peaks at 2918 and 2850  $\text{cm}^{-1}$  are

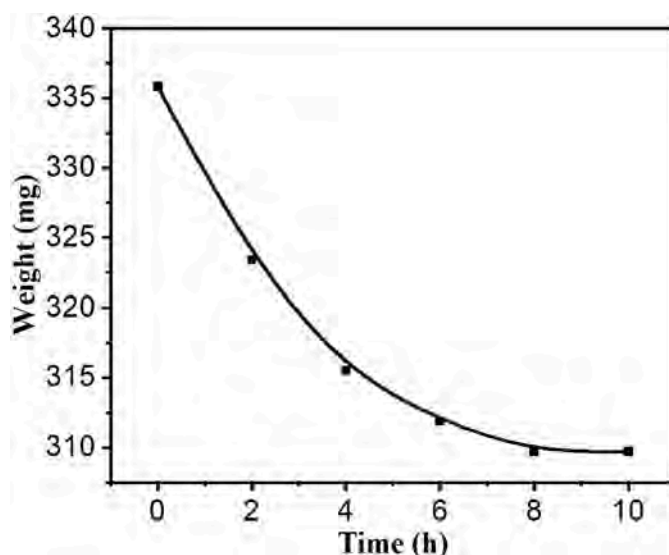


Fig. 2. The quality of PW@CNS at different leak times.

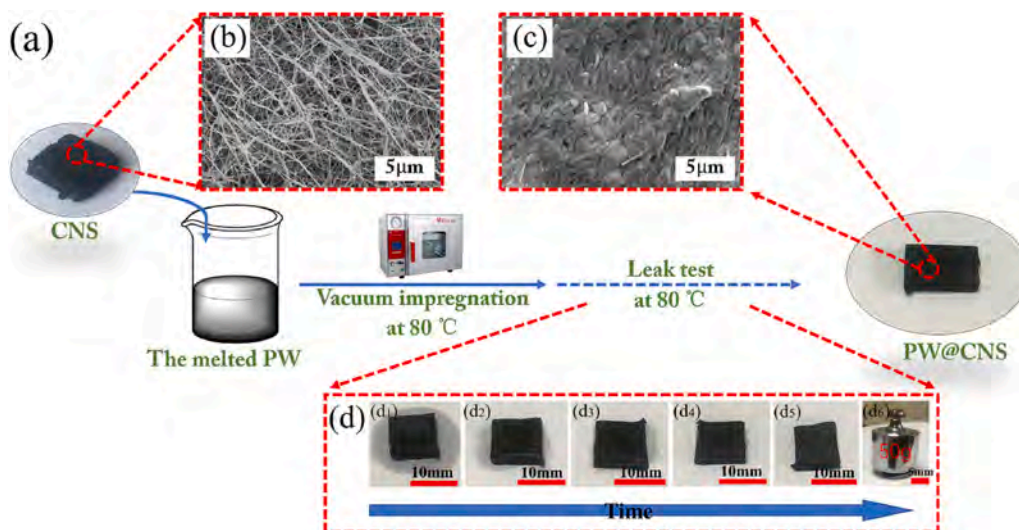


Fig. 1. (a) Schematic diagram for the preparation of PW@CNS, the SEM images of (b) CNS and (c) PW@CNS, (d) the digital pictures of leakage test for PW@CNS



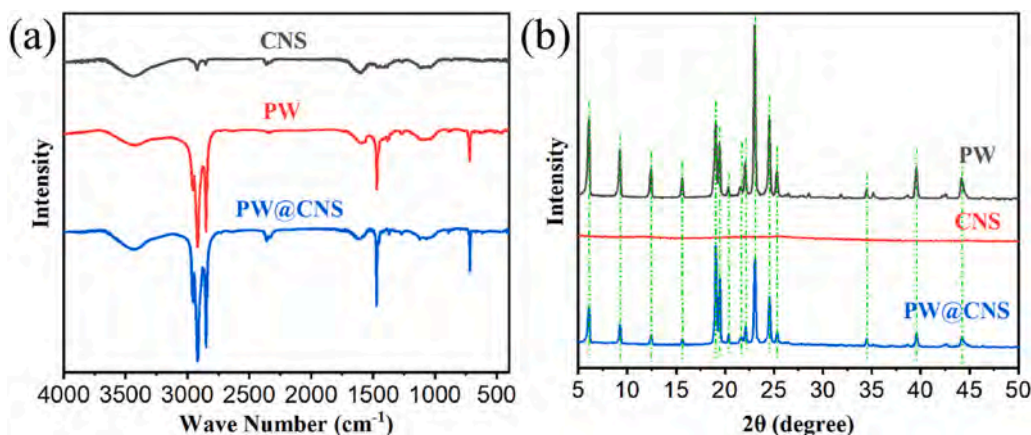


Fig. 3. (a) The FTIR spectra and (b) XRD patterns of CNS, pure PW and PW@CNS

attributed to the C–H asymmetric stretching and symmetric vibration, respectively, and the characteristic peaks at  $1470$  and  $720\text{ cm}^{-1}$  are attributed to the C–H bending vibration and  $\text{CH}_2$  rocking vibration, respectively [12,40]. For CNSs, the peaks appearing at  $2927$  and  $2852\text{ cm}^{-1}$  are attributed to the stretching absorption of –C–H, and the peak at  $1602\text{ cm}^{-1}$  can be attributed to the stretching absorption of –C=C– [41]. However, through comparison, it is found that the FTIR spectra of PW@CNS is just a simple physical superposition of the FTIR spectra of PW and CNS, and no new characteristic peak and/or significant peak shift are observed. It indicates that there is no any chemical but only physical interaction between PW and CNS, such as capillary adsorption, Vander Waals forces and hydrogen bond, etc., during the vacuum impregnation processing.

Furthermore, in order to study the effect of CNS on the crystallization performance of PW, the XRD patterns of pure PW, CNS and PW@CNS are provided in Fig. 3 (b). On the one hand, the sharp diffraction peaks

appeared at about  $6.1^\circ$ ,  $9.3^\circ$ ,  $12.5^\circ$ ,  $15.6^\circ$ ,  $19.1^\circ$ ,  $19.5^\circ$ ,  $22.1^\circ$ ,  $23.1^\circ$ ,  $24.5^\circ$ ,  $25.3^\circ$ ,  $39.6^\circ$  and  $44.2^\circ$  are ascribed to the (110), (200), and some other crystal planes of PW [42], which indicates that the PW has a good crystallization capability. On the other hand, the CNS pattern shows only a flat diffraction peak at approximately  $25.0^\circ$  due to its poor crystallization capability. After combining PW and CNS, the PW@CNS pattern shows similar peaks to pure PW, suggesting that, even in the presence of CNS, the crystal structure of the PW segments in PW@CNS remains. Although no new peak appears in the PW@CNS pattern, the peak intensity of PW component in PW@CNS is obviously lower than that of pure PW. This indicates that the crystalline region of PW molecular chain in the PW@CNS composite is affected and reduced to some extent due to the restriction of reticulated CNS. Hence, both the FTIR and XRD results confirm that there is no chemical interaction but only physical interaction occurs between PW and CNS.

DSC is one of the most effective methods for characterizing the

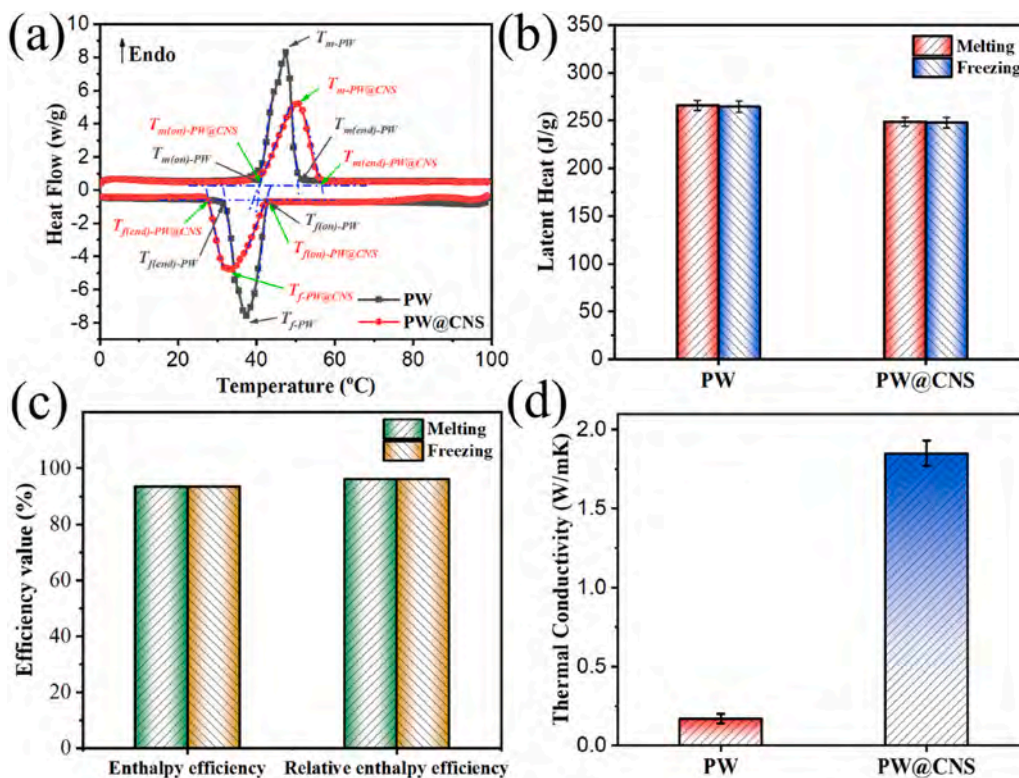


Fig. 4. (a) The DSC curves of PW and PW@CNS, the corresponding (b) latent heat of PW and PW@CNS, (c) efficiency of PW@CNS, (d) thermal conductivity of PW and PW@CNS

thermal energy storage behavior of PCMs. The DSC curves and corresponding melting latent heat ( $\Delta H_m$ ), freezing latent heat ( $\Delta H_f$ ), enthalpy efficiency ( $\alpha$ ) and relative enthalpy efficiency ( $\eta$ ) of pure PW and the obtained PW@CNS are shown in Fig. 4 (a)-(c). The corresponding melting temperature and freezing temperature, including melting onset temperature ( $T_{m(on)}$ ), melting peak temperature ( $T_m$ ), melting end temperature ( $T_{m(end)}$ ), freezing onset temperature ( $T_{f(on)}$ ), freezing peak temperature ( $T_f$ ), freezing end temperature ( $T_{f(end)}$ ), melting temperature range ( $\Delta T_m = T_{m(end)} - T_{m(on)}$ ) and freezing temperature range ( $\Delta T_f = T_{f(on)} - T_{f(end)}$ ) are listed in Table 1. In this study, the  $\Delta H_m$  and  $\Delta H_f$  are the peak areas of the melting and freezing curves, and  $\alpha$  and  $\eta$  are calculated by Eqs. (4) and (5), respectively. The larger  $\alpha$  and  $\eta$  values represent the smaller latent heat loss.

$$\alpha = \frac{\Delta H_{m(PW@CNS)}}{\Delta H_{m(PW)}} \times 100\% \quad (4)$$

$$\eta = \frac{\Delta H_{m(PW@CNS)}}{\Delta H_{m(PW)} \times w_f} \times 100\% \quad (5)$$

where  $w_f$  is the PW loading in the obtained PW@CNS composites.

As shown in Fig. 4 (a), both pure PW and PW@CNS go through similar melting and freezing processes from 20 °C to 60 °C. Pure PW and PW@CNS have almost the same  $T_{m(on)}$  and  $T_{f(on)}$ . However, compared to pure PW (9.6 °C and 11.0 °C), the  $\Delta T_m$  (15.9 °C) and  $\Delta T_f$  (15.1 °C) of PW@CNS are wider with the introduction of CNS, and accordingly, the  $T_m$  and  $T_f$  of PW@CNS also show a small increase and decrease, respectively. This indicates that the crystallization process of PW molecular chain in PW@CNS composite is affected by CNS, which is in agreement with the XRD results. In addition, the  $\Delta H_m$  and  $\Delta H_f$  of PW@CNS are as high as 248.8 J/g and 247.7 J/g, respectively, due to the high PW loading in PW@CNS, these values are quite close to those of pure PW (265.8 J/g and 264.5 J/g, respectively) (Fig. 4 b). In addition, the  $\alpha$  and  $\eta$  values of PW@CNS during the thermal energy storage process (melting process) are 93.5% and 96.2%, and the  $\alpha$  and  $\eta$  values of PW@CNS during the thermal energy release process (freezing process) are 93.6% and 96.3% (Fig. 4 c), respectively. As shown in Table 2, the  $\alpha$  and  $\eta$  values of PW@CNS both in the thermal energy storage and release processes are higher than most of the previously reported values. Thus, compared to pure PW, the PW@CNS composite prepared via simple vacuum impregnation just lost a small amount latent heat, and exhibits the excellent thermal energy storage capacity.

Fig. 4 (d) shows the thermal conductivity ( $\lambda$ ) of pure PW and PW@CNS. Pure PW is the bad conductor of heat. Therefore, its  $\lambda$  value is as low as 0.17 W/mK. However, the  $\lambda$  value of PW@CNS increases to 1.85 W/mK, which is about 11 times that of pure PW. The higher  $\lambda$  value corresponds to higher thermal energy storage and release rates. The  $\lambda$  value of the obtained PW@CNS is higher than most of the reported PW-based FSPCMs (Table 2), probably because the PW@CNS composite has a complete carbon nanotube skeleton with high thermal conductivity, which is not damaged during the composite preparation process.

**Table 1**  
The melting and freezing temperature parameters of PW and PW@CNS

Samples	$T_{m(on)}$ (°C)	$T_m$ (°C)	$T_{m(end)}$ (°C)	$\Delta T_m$ (°C)	$T_{f(on)}$ (°C)	$T_f$ (°C)	$T_{f(end)}$ (°C)	$\Delta T_f$ (°C)
PW	40.8	47.4	50.4	9.6	42.8	37.4	31.8	11.0
PW@CNS	40.8	50.8	56.7	15.9	42.8	32.9	27.7	15.1

\*  $T_{m(on)}$ : melting onset temperature.

$T_m$ : melting peak temperature.

$T_{m(end)}$ : melting end temperature.

$\Delta T_m$ : melting temperature range.

$T_{f(on)}$ : freezing onset temperature.

$T_f$ : freezing peak temperature.

$T_{f(end)}$ : freezing end temperature.

$\Delta T_f$ : freezing temperature range.

**Table 2**

The  $\lambda$ ,  $\eta$  and  $\lambda$  values of PW-based FSPCMs in the literature.

PW-based FSPCMs	melting process		freezing process		$\lambda$ (W/mK)	Refs
	$\alpha$ (%)	$\eta$ (%)	$\alpha$ (%)	$\eta$ (%)		
PW/CAN800	57.7	96.2	53.4	89.0	0.52	[40]
PW/EG/SR	25.3	93.7	24.6	91.1	0.56	[43]
PW/MF/RGO	87.8	92.4	92.9	97.8	–	[13]
PW/HCF	69.1	98.7	67.1	95.8	0.53	[16]
PW/HCF	88.3	101.3	88.7	101.7	1.73	[44]
PW/HPC	70.8	93.3	70.9	93.4	0.48	[45]
PW/CNS	93.5	96.2	93.6	96.3	1.85	This work

\* $\alpha$ : enthalpy efficiency.

$\eta$ : relative enthalpy efficiency.

$\lambda$ : thermal conductivity.

Therefore, the obtained PW@CNS composite with excellent thermal energy storage capacity and improved thermal conductivity will have applications in the field of thermal management of various electronic devices.

For the long-term use of the FSPCMs, it is important to improve their thermal reliability and reusability. Fig. 5 (a) and (b) show the DSC curves and XRD patterns of PW@CNS before and after 100 thermal cycles, respectively. The corresponding  $\Delta H_m$  and  $\Delta H_f$  before and after 100 thermal cycles are listed in Table 3. At the same time, the relative coefficients ( $\delta_m$ ) and ( $\delta_f$ ) are used to evaluate the loss of  $\Delta H_m$  and  $\Delta H_f$  before and after 100 thermal cycles by Eqs. (6) and (7), respectively. The lower  $\delta_m$  and  $\delta_f$  values, the better thermal reliability and reusability.

$$\delta_m = \frac{\Delta H_{m(before)} - \Delta H_{m(after)}}{\Delta H_{m(before)}} \times 100\% \quad (6)$$

$$\delta_f = \frac{\Delta H_{f(before)} - \Delta H_{f(after)}}{\Delta H_{f(before)}} \times 100\% \quad (7)$$

As shown in Fig. 5 (a), the DSC curves of PW@CNS before and after 100 thermal cycles almost overlap. The corresponding  $\Delta H_m$  and  $\Delta H_f$  of PW@CNS after 100 thermal cycles (247.9 J/g and 246.4 J/g, respectively) are very close to those before thermal cycles (248.8 J/g and 247.7 J/g). Thus, the calculated  $\delta_m$  and  $\delta_f$  values are as low as 0.4% and 0.5%, respectively. In addition, from Fig. 5 (b), after 100 thermal cycles, the XRD patterns of PW@CNS present the same characteristic band positions as those obtained before the cycling test. Therefore, the obtained PW@CNS has good thermal reliability and reusability for long-term practical utility.

The thermal stability is another important parameter of FSPCMs for practical applications. Fig. 6 shows the TGA curves of pure PW, CNS and PW@CNS. Compared with pure PW, the CNS has good thermal stability, as it exhibits almost no weight loss within 600 °C. For pure PW, the 5 wt % weight loss appears at 160.3 °C ( $T_5$ ), and the maximum degradation temperature ( $T_{max}$ ) is about 230.2 °C. With the introduction of CNS, the  $T_5$  and  $T_{max}$  of PW@CNS increase to 193.4 °C and 268.5 °C, respectively, which are much higher than those of PW (47.4 °C and 37.4 °C).

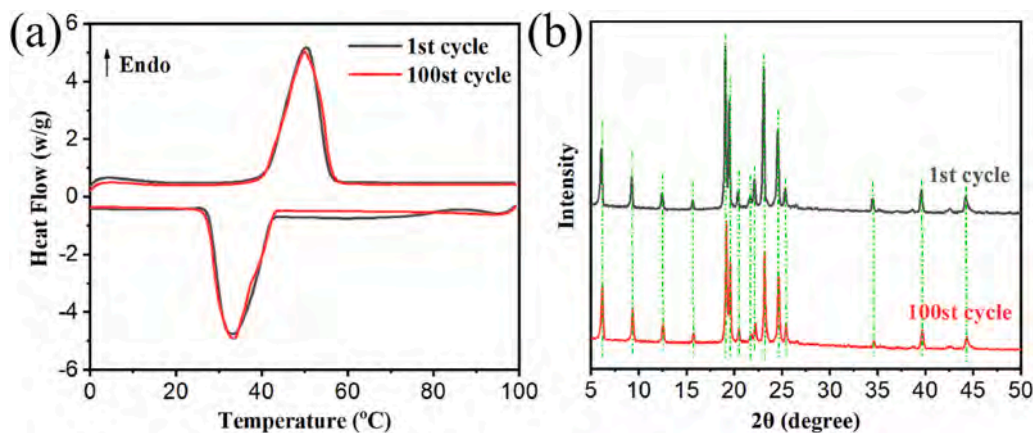


Fig. 5. (a) DSC curves and (b) XRD patterns of PW@CNS before and after 100 thermal cycles.

Table 3

The thermal parameters of PW@CNS before and after 100 thermal cycles.

PW@CNS	$\Delta H_m$ (J/g)	$\delta_m$ (%)	$\Delta H_f$ (J/g)	$\delta_f$ (%)
Before	248.8	–	247.7	–
After	247.9	0.4	246.4	0.5

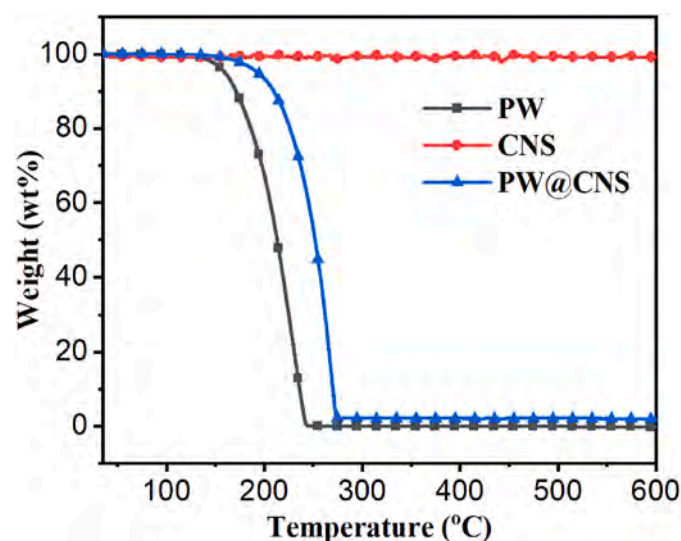


Fig. 6. The TGA curves of pure PW, CNS and PW@CNS

Moreover, within 100 °C, there is almost no weight loss for PW@CNS. This indicates that the PW@CNS has good thermal stability in the phase change temperature range.

### 3.2. Thermal management behavior of PW@CNS

As described above, the obtained PW@CNS composites has excellent thermal energy storage capacity, good thermal reliability, reusability and stability. In theory, the obtained PW@CNS composite is expected to show excellent thermal management capabilities for applications in electronic devices. Therefore, a simulated thermal management experiment was designed to verify these capabilities, as shown in Fig. 7. In order to simplify the experiment, we use a heat source with temperature set at 70 °C to heat the simulated electronic device to simulating the temperature increase process of the electronic devices due to its high speed and efficiency operation. In Fig. 7, the temperature change of point 2 (without PW@CNS) is the temperature change of the electronic device itself. For comparison, a piece of PW@CNS is placed at point 1, and the temperature change of point 1 (with PW@CNS) is the temperature change of the electronic device after thermal management via PW@CNS. Throughout the experiment, the temperature changes at points 1 and 2 are monitored using infrared cameras and recorded with a data collector.

Fig. 8 shows the thermal infrared images of the above simulated thermal management process at different times, and Fig. 9 shows the corresponding temperature-time curves for points 1 and 2. In Fig. 8, the blue portion represents the low temperature and the red or even white portion represents the high temperature. In the beginning (Fig. 8 a), the temperatures at points 1 and 2 are close to the ambient temperature, so all the portion with or without PW@CNS are blue. As the simulated electronic device is heated, its temperature increases rapidly and its color changes quickly to yellow or even red (Fig. 8 b). From Fig. 9, after

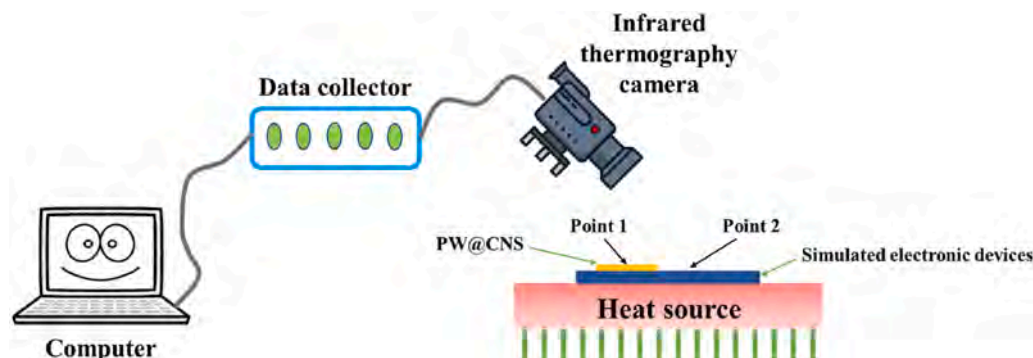


Fig. 7. The schematic illustration for thermal management behavior of PW@CNS



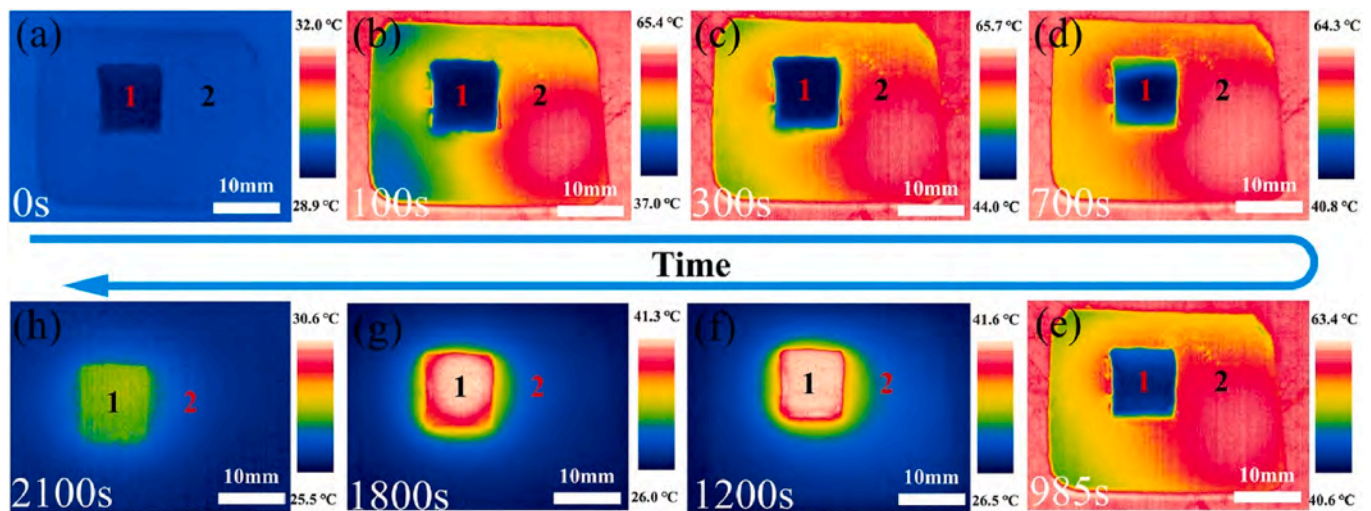


Fig. 8. The thermal infrared images of thermal management process with different time.

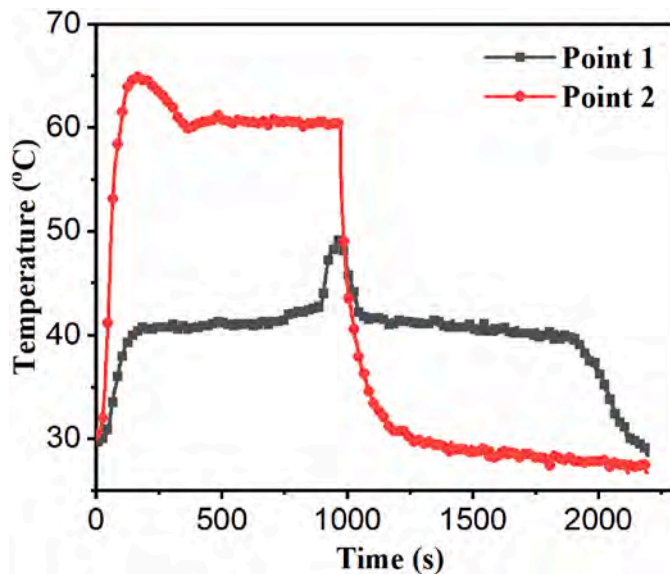


Fig. 9. The temperature-time curves of points 1 and 2 during the thermal management process.

the temperature at point 2 reaches the maximum (about 65 °C), due to thermal diffusion and other factors, the temperature at point 2 first drops slowly and then reaches an endothermic/exothermic equilibrium state, where it remains at 60 °C (Fig. 8 c, d, and e). However, for point 1, due to the phase transition process of the PW component in the PW@CNS composite, the temperature remains at around 40 °C for a long time (from 150 s to 900 s) and then rapidly rises to 41 °C. During this process, the PW component in PW@CNS is constantly going through a “solid-liquid” phase transition and storing the corresponding melting latent heat. Thus, in the electronic device, the temperature of the portion with PW@CNS is significantly lower than that of the portion without PW@CNS. Correspondingly, in Fig. 8(b–d), the color of the portion with PW@CNS is bluer than that of the portion without PW@CNS. At about 900 s, the PW component in PW@CNS has completed the “solid-liquid” phase transition, and the temperature at point 1 continues to rise slowly. Then, the heat source is turned off and the device is quickly cooled for about 1000 s. The temperature at point 2 also drops rapidly and eventually reaches room temperature. However, the temperature at point 1 remains stable at about 41 °C for a long time (from 1050 s to 1900 s) due to the “liquid-solid” phase transition. Correspondingly, in Fig. 8(f–h),

the color of portion with PW@CNS is redder than that portion without PW@CNS. Throughout the experiment, the temperature at point 2 is above 60 °C for a long time and it varies by up to 30 °C. However, if the temperature at point 1 can be maintained at around 40 °C for a long time, it will be more conducive to the long-term efficient operation of electronic devices at their optimal operating temperature. All the above results show that the use of FSPCMs for the thermal management of electronic devices is a very efficient choice.

### 3.3. EMI SE and microwave absorption performance of PW@CNS

Conductive network with super high electrical conductivity plays a prominent role in the attenuation of electromagnetic radiation. Fig. 10 (a) shows the electrical conductivity of pure PW, CNS and PW@CNS, and Fig. 10 (b) and (c) show the EMI SE of pure PW and PW@CNS, respectively. Pure PW is an electrical insulator, so its electrical conductivity is as low as  $10^{-13}$  S/m. For CNS, due to its good three-dimensional structure and the excellent electrical conductivity of carbon nanotubes, its electrical conductivity is as high as 400 S/m. After combining PW and CNS, the electrical conductivity of PW@CNS is still as high as 30 S/m, which can be attributed to the completed three-dimensional conductive path constructed by carbon nanotubes with high electrical conductivity. Therefore, due to the lower electrical conductivity, the EMI SE of pure PW is almost zero. For PW@CNS, according to the S-parameters, the average values of reflection coefficient (R), transmission coefficient (T) and absorption coefficient (A) of PW@CNS are 0.66, 0.01 and 0.33 in the frequency of 1.0–18.0 GHz, respectively. In addition, its SE of reflection ( $SE_R$ ) hardly changes with the electromagnetic wave frequency, however, the SE of absorption ( $SE_A$ ) generally increases with the frequency between 1.0 GHz and 18.0 GHz. Thus, the total SE ( $SE_T$ ) of PW@CNS also generally increases with increasing frequency in the range of test frequency. The average  $SE_R$ ,  $SE_A$  and  $SE_T$  are 4.7, 17.6 and 22.3 dB in the range of 1.0–18.0 GHz, respectively, which is sufficient for most commercial application scenarios. Furthermore, the average  $SE_A$  and  $SE_T$  in the high-frequency region are greater than that in the low-frequency region and even over the entire test frequency range. For example, the average  $SE_A$  and  $SE_T$  in the range of 13.0–18.0 GHz are as high as 24.9 and 29.4 dB, respectively. Obviously, the  $SE_A$  value of PW@CNS is much larger than its  $SE_R$  value in the range of test frequency, which indicates that the proportion of the absorbed electromagnetic wave energy is much higher than that of the reflected electromagnetic wave energy, which is assistant with most of the reported literatures [24,26,46–48]. All the results indicate that the obtained PW@CNS is a highly efficient electromagnetic shielding

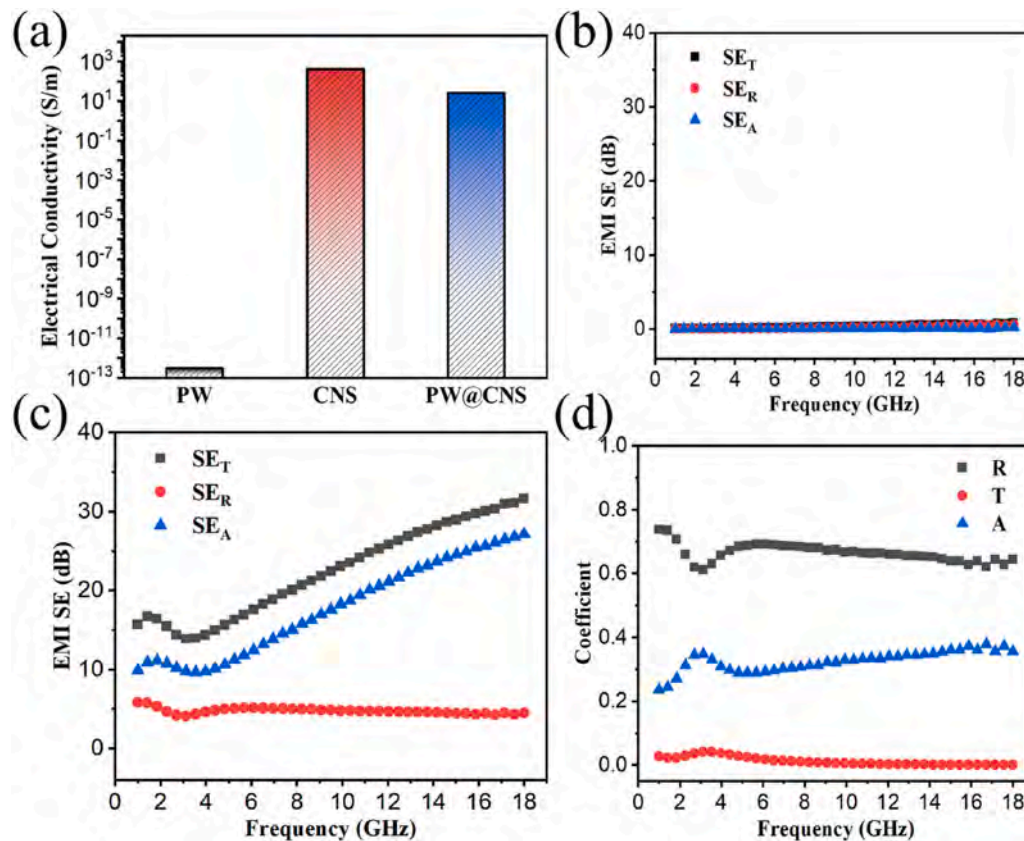


**Fig. 10.** (a) The electrical conductivities of pure PW, CNS and PW@CNS, the EMI SE of (b) pure PW and (c) PW@CNS, the reflection coefficient, transmission coefficient and absorption coefficient of PW@CNS within the test frequency range.

material, whose effectiveness is mainly based on the absorption of electromagnetic waves, and it can be used in the most commercial application scenarios.

Finally, considering its excellent thermal management capabilities and good electromagnetic interference shielding effectiveness, the obtained PW@CNS is expected to achieve the long-term efficient operation of electronic devices at lower temperatures while shielding against electromagnetic wave interference and radiation pollution, which has a very high commercial value.

#### 4. Conclusion

In this study, the PW@CNS composite with simultaneous high-efficient thermal management and electromagnetic interference shielding functions was successfully prepared via the simple vacuum impregnation method. In the PW@CNS composite, the PW component is employed as the phase change working substance for thermal management applications and the three-dimensional conductive CNS component is employed to support matrix for PW and as a shield against electromagnetic waves. Due to the excellent adsorption capacity of CNS for PW, the mass of fraction of PW in PW@CNS is as high as 97.2 wt%. Thus, the latent heat of PW@CNS during the melting and freezing process are 248.8 J/g and 247.7 J/g, respectively, which are very close to those of pure PW. The corresponding enthalpy efficiencies (93.5% and 93.6%) and relative enthalpy efficiency (96.2% and 96.3%) of PW@CNS during the melting and freezing process are higher than most of the previously reported values. The latent heat values of PW@CNS before and after 100 thermal cycles are very similar. It indicates the obtained PW@CNS has good thermal reliability and reusability. Due to the excellent thermal energy storage capability, the temperature of an electronic device managed by PW@CNS can be maintained at 41 °C for a long time, facilitating the long-term efficient operation of the electronic

device at its optimal temperature environment. In addition, the PW@CNS offers very effective shielding against electromagnetic interference. In conclusion, the obtained PW@CNS has great potential in the field of thermal management and electromagnetic interference shielding for electronic devices.

#### Author statement

Xiang Lu: Methodology, Validation, Investigation, Data Curation, Writing - Original Draft, Writing - Review & Editing. Yongfeng Zheng: Formal analysis, Investigation. Jinglei Yang: Conceptualization, Resources, Writing - Review & Editing, Supervision, Project administration. Jinping Qu: Formal analysis, Writing - Review & Editing, Funding acquisition.

#### Declaration of competing interest

The authors declare that they have no known competing financial interests or personal relationships that could have appeared to influence the work reported in this paper.

#### Acknowledgements

The authors acknowledge support from the National Natural Science Foundation of China (Grant No. 51903092), the China Postdoctoral Science Foundation funded project (Grant No. 2019M652884), the National Key Research and Development Program of China (Grant No. 2016YFB0302300) and the Natural Science Foundation of Guangdong Province (2018A030313275).



## References

- [1] Yin C-G, Liu Z-J, Mo R, Fan J-C, Shi P-H, Xu Q-J, et al. Copper nanowires embedded in boron nitride nanosheet-polymer composites with enhanced thermal conductivities for thermal management. *Polymer* 2020;195:122455.
- [2] Guo F, Shen X, Zhou J, Liu D, Zheng Q, Yang J, et al. Highly thermally conductive dielectric nanocomposites with synergistic alignments of graphene and boron nitride nanosheets. *Adv Funct Mater* 2020;30:1910826.
- [3] Li X, Li C, Zhang X, Jiang Y, Xia L, Wang J, et al. Simultaneously enhanced thermal conductivity and mechanical properties of PP/BN composites via constructing reinforced segregated structure with a trace amount of BN wrapped PP fiber. *Chem Eng J* 2020;390:124563.
- [4] Nan B, Wu K, Qu Z, Xiao L, Xu C, Shi J, et al. A multifunctional thermal management paper based on functionalized graphene oxide nanosheets decorated with nanodiamond. *Carbon* 2020;161:132–45.
- [5] Cao H, Tan Z, Fan G, Guo Q, Su Y, Li Z, et al. Wide and fine alignment control and interface modification for high-performance thermally conductive graphite/copper composite. *Compos B Eng* 2020;191:107965.
- [6] Yang X, Zhu J, Yang D, Zhang J, Guo Y, Zhong X, et al. High-efficiency improvement of thermal conductivities for epoxy composites from synthesized liquid crystal epoxy followed by doping BN fillers. *Compos B Eng* 2020;185: 107784.
- [7] Song J, Zhang Y. Vertically aligned silicon carbide nanowires/reduced graphene oxide networks for enhancing the thermal conductivity of silicone rubber composites. *Compos Part A-Appl S* 2020;133:105873.
- [8] Li M, Wang M, Hou X, Zhan Z, Wang H, Fu H, et al. Highly thermal conductive and electrical insulating polymer composites with boron nitride. *Compos B Eng* 2020; 184:107746.
- [9] Lu X, Liang B, Sheng X, Yuan T, Qu J. Enhanced thermal conductivity of polyurethane/wood powder composite phase change materials via incorporating low loading of graphene oxide nanosheets for solar thermal energy storage. *Sol Energy Mater Sol Cell* 2020;208:110391.
- [10] Jia X, Li Q, Ao C, Hu R, Xia T, Xue Z, et al. High thermal conductive shape-stabilized phase change materials of polyethylene glycol/boron nitride@chitosan composites for thermal energy storage. *Compos Part A-Appl S* 2020;129:105710.
- [11] Lu X, Huang J, Wong W-Y, Qu J-p. A novel bio-based polyurethane/wood powder composite as shape-stable phase change material with high relative enthalpy efficiency for solar thermal energy storage. *Sol Energy Mater Sol Cell* 2019;200: 109987.
- [12] Zhu X, Han L, Yang F, Jiang J, Jia X. Lightweight mesoporous carbon fibers with interconnected graphitic walls for supports of form-stable phase change materials with enhanced thermal conductivity. *Sol Energy Mater Sol Cell* 2020;208:110361.
- [13] Wu H-y, Li S-t, Shao Y-w, Jin X-z, Qi X-d, Yang J-h, et al. Melamine foam/reduced graphene oxide supported form-stable phase change materials with simultaneous shape memory property and light-to-thermal energy storage capability. *Chem Eng J* 2020;379:122373.
- [14] Zhang X, Zhu C, Fang G. Preparation and thermal properties of n-eicosane/nano-SiO<sub>2</sub>/expanded graphite composite phase-change material for thermal energy storage. *Mater Chem Phys* 2020;240:122178.
- [15] Wang Q, Zhou D, Chen Y, Eames P, Wu Z. Characterization and effects of thermal cycling on the properties of paraffin/expanded graphite composites. *Renew Energy* 2020;147:1131–8.
- [16] Umair MM, Zhang Y, Tehrim A, Zhang S, Tang B. Form-stable phase-change composites supported by a biomass-derived carbon scaffold with multiple energy conversion abilities. *Ind Eng Chem Res* 2020;59:1393–401.
- [17] Zhou Y, Li C, Wu H, Guo S. Construction of hybrid graphene oxide/graphene nanoplates shell in paraffin microencapsulated phase change materials to improve thermal conductivity for thermal energy storage. *Colloids Surf, A* 2020;597: 124780.
- [18] Ma B, Chen S-s, Ren Y-z, Zhou X-y. The thermoregulation effect of microencapsulated phase-change materials in an asphalt mixture. *Construct Build Mater* 2020;231:117186.
- [19] Ding Z, He F, Li Y, Jiang Z, Yan H, He R, et al. Novel shape-stabilized phase change materials based on paraffin/EPDM@graphene with high thermal conductivity and low leakage rate. *Energy Fuel* 2020;34:5024–31.
- [20] Chen Y, Gao S, Liu C, Situ Y, Liu J, Huang H. Preparation of PE-EPDM based phase change materials with great mechanical property, thermal conductivity and photo-thermal performance. *Sol Energy Mater Sol Cell* 2019;200:109988.
- [21] Tang Y, Jia Y, Alva G, Huang X, Fang G. Synthesis, characterization and properties of palmitic acid/high density polyethylene/graphene nanoplatelets composites as form-stable phase change materials. *Sol Energy Mater Sol Cell* 2016;155:421–9.
- [22] Zhang H, Jia Z, Feng A, Zhou Z, Zhang C, Wang K, et al. Enhanced microwave absorption performance of sulfur-doped hollow carbon microspheres with mesoporous shell as a broadband absorber. *Compos Commun* 2020;19:42–50.
- [23] Fu H, Yang Z, Zhang Y, Zhu M, Jia Y, Chao Z, et al. SWCNT-modulated folding-resistant sandwich-structured graphene film for high-performance electromagnetic interference shielding. *Carbon* 2020;162:490–6.
- [24] Li J, Ding Y, Gao Q, Zhang H, He X, Ma Z, et al. Ultrathin and flexible biomass-derived C@CoFe nanocomposite films for efficient electromagnetic interference shielding. *Compos B Eng* 2020;190:107935.
- [25] Zhu S, Cheng Q, Yu C, Pan X, Zuo X, Liu J, et al. Flexible Fe<sub>3</sub>O<sub>4</sub>/graphene foam/poly dimethylsiloxane composite for high-performance electromagnetic interference shielding. *Compos Sci Technol* 2020;189:108012.
- [26] Zhou ZH, Li MZ, Huang HD, Li L, Yang B, Yan DX, et al. Structuring hierarchically porous architecture in biomass-derived carbon aerogels for simultaneously achieving high electromagnetic interference shielding effectiveness and high absorption coefficient. *ACS Appl Mater Interfaces* 2020;12:18840–9.
- [27] Liang C, Qiu H, Song P, Shi X, Kong J, Gu J. Ultra-light MXene aerogel/wood-derived porous carbon composites with wall-like “mortar/brick” structures for electromagnetic interference shielding. *Sci Bull* 2020;65:616–22.
- [28] Wang YY, Zhou ZH, Zhou CG, Sun WJ, Gao JF, Dai K, et al. Lightweight and robust Carbon nanotube/Polyimide foam for efficient and heat-resistant electromagnetic interference shielding and microwave absorption. *ACS Appl Mater Interfaces* 2020; 12:8704–12.
- [29] Liang L, Zhang Z, Song F, Zhang W, Li H, Gu J, et al. Ultralight, flexible carbon hybrid aerogels from bacterial cellulose for strong microwave absorption. *Carbon* 2020;162:283–91.
- [30] Jia H, Kong Q-Q, Liu Z, Wei X-X, Li X-M, Chen J-P, et al. 3D graphene/carbon nanotubes/polydimethylsiloxane composites as high-performance electromagnetic shielding material in X-band. *Compos Part A-Appl S* 2020;129:105712.
- [31] Gui X, Wei J, Wang K, Cao A, Zhu H, Jia Y, et al. Carbon nanotube sponges. *Adv Mater* 2010;22:617–21.
- [32] Bang J, You DW, Jang Y, Oh JS, Jung KW. A carbon nanotube sponge as an adsorbent for vapor preconcentration of aromatic volatile organic compounds. *J Chromatogr A* 2019;1605:460363.
- [33] Jang Y, Bang J, Seon YS, You DW, Oh JS, Jung KW. Carbon nanotube sponges as an enrichment material for aromatic volatile organic compounds. *J Chromatogr A* 2020;1617:460840.
- [34] Kukkar D, Rani A, Kumar V, Younis SA, Zhang M, Lee SS, et al. Recent advances in carbon nanotube sponge-based sorption technologies for mitigation of marine oil spills. *J Colloid interf Sci* 2020;570:411–22.
- [35] Chen L, Zou R, Xia W, Liu Z, Shang Y, Zhu J, et al. Electro- and photodriven phase change composites based on wax-infiltrated carbon nanotube sponges. *ACS Nano* 2012;6:10884–92.
- [36] Zhang F, Feng Y, Qin M, Ji T, Lv F, Li Z, et al. Stress-sensitive thermally conductive elastic nanocomposite based on interconnected graphite-welded carbon nanotube sponges. *Carbon* 2019;145:378–88.
- [37] Zhang F, Feng Y, Qin M, Gao L, Li Z, Zhao F, et al. Stress controllability in thermal and electrical conductivity of 3D elastic graphene-crosslinked carbon nanotube sponge/polyimide nanocomposite. *Adv Funct Mater* 2019;29:1901383.
- [38] Chen Y, Zhang H-B, Yang Y, Wang M, Cao A, Yu Z-Z. High-performance epoxy nanocomposites reinforced with three-dimensional carbon nanotube sponge for electromagnetic interference shielding. *Adv Funct Mater* 2016;26:447–55.
- [39] Lu D, Mo Z, Liang B, Yang L, He Z, Zhu H, et al. Flexible, lightweight carbon nanotube sponges and composites for high-performance electromagnetic interference shielding. *Carbon* 2018;133:457–63.
- [40] Zuo X, Li J, Zhao X, Yang H, Chen D. Emerging paraffin/carbon-coated nanoscroll composite phase change material for thermal energy storage. *Renew Energy* 2020; 152:579–89.
- [41] Sari A, Al-Ahmed A, Bicer A, Al-Sulaiman FA, Hekimoğlu G. Investigation of thermal properties and enhanced energy storage/release performance of silica fume/myristic acid composite doped with carbon nanotubes. *Renew Energy* 2019; 140:779–88.
- [42] Wu W, Wu W, Wang S. Form-stable and thermally induced flexible composite phase change material for thermal energy storage and thermal management applications. *Appl Energy* 2019;236:10–21.
- [43] Zhang Y, Li W, Huang J, Cao M, Du G. Expanded graphite/paraffin/silicone rubber as high temperature form-stabilized phase change materials for thermal energy storage and thermal interface materials. *Materials* 2020;13:894.
- [44] Sheng N, Rao Z, Zhu C, Habazaki H. Honeycomb carbon fibers strengthened composite phase change materials for superior thermal energy storage. *Appl Therm Eng* 2020;164:114493.
- [45] Sun Keyan, Yan Kou, Zhang Yanwei, Liu Tingting, Shi Q. Photo-triggered hierarchical porous carbon based composite phase change materials with superior thermal energy conversion capacity. *ACS Sustainable Chem Eng* 2020;8:3445–53.
- [46] Yim Y-J, Rhee KY, Park S-J. Electromagnetic interference shielding effectiveness of nickel-plated MWCNTs/high-density polyethylene composites. *Compos B Eng* 2016;98:120–5.
- [47] Singh AK, Shishkin A, Koppel T, Gupta N. A review of porous lightweight composite materials for electromagnetic interference shielding. *Compos B Eng* 2018;149:188–97.
- [48] Zhang H, Zhang G, Li J, Fan X, Jing Z, Li J, et al. Lightweight, multifunctional microcellular PMMA/Fe<sub>3</sub>O<sub>4</sub> @MWCNTs nanocomposite foams with efficient electromagnetic interference shielding. *Compos Part A-Appl S* 2017;100:128–38.